



The influence of supported Ni catalysts on the product gas distribution and H₂ yield during cellulose pyrolysis

Ming Zhao^a, Nicholas H. Florin^b, Andrew T. Harris^{a,*}

^a Laboratory for Sustainable Technology, School of Chemical and Biomolecular Engineering, The University of Sydney, NSW 2006, Australia

^b Grantham Institute for Climate Change, The Imperial College, South Kensington Campus, London SW7 2AZ, United Kingdom

ARTICLE INFO

Article history:

Received 16 March 2009

Received in revised form 13 July 2009

Accepted 14 July 2009

Available online 18 July 2009

Keywords:

Cellulose pyrolysis

H₂ yield

Supported Ni catalyst

γ -Al₂O₃

MCM-41

ABSTRACT

Two groups of Ni catalysts, supported on γ -Al₂O₃ and MCM-41, respectively, were prepared by incipient wetness impregnation and tested for their influence on the pyrolytic decomposition of cellulose. A thermogravimetric analyser coupled with a mass spectrometer (TG–MS) was used to examine the influence of catalyst loading, support material, and the presence of additional water vapour on H₂ selectivity. Normalization of the raw MS data enabled semi-quantitative analysis of the product gas distribution, which facilitated reliable comparison between different experimental conditions. Catalysts were characterized by BET, XRD, SEM/EDX and TEM. MCM-41 supported Ni significantly elevated the yield of H₂ and total gaseous product, both under Ar and with the injection of additional water vapour when compared with the γ -Al₂O₃ support. 15 wt.%Ni/ γ -Al₂O₃ and 5 wt.%Ni/MCM-41 were identified as the most active catalysts from the two groups with regards to H₂ selectivity and yield.

© 2009 Elsevier B.V. All rights reserved.

1. Introduction

Hydrogen (H₂) from non-edible biomass has received attention as a sustainable and renewable alternative to fossil fuels. Of the techniques available to synthesize hydrogen sustainably, the pyrolysis and gasification of biomass show promise as being of sufficient scale to satisfy future demand [1–3]. During pyrolysis or gasification, the chain structure of lignocellulosic biomass is decomposed, with the evolved gas species undergoing secondary cracking and reforming reactions yielding a H₂-rich product gas, non-degradable tars and char residues [4].

Tar cracking and steam reforming reactions are typically endothermic and favour high gasification temperatures whereas the water–gas shift reaction is exothermic; thus, there is a tradeoff in terms of the gasification temperature that is optimal for promoting the decomposition of the higher hydrocarbons (>C₃) and the water–gas shift reaction [5]. With the use of selective catalysts, it becomes possible to degrade the tars and promote the reforming reactions at temperatures suitable for the water–gas shift reaction, thus generating a product gas consisting mainly of H₂ and CO₂, with a low CO content [6,7]. If CO₂ is removed from the system continuously, then the remaining H₂ is at a high concentration, theoretically >80% (dry) [8] with the possibility of use in a fuel cell.

Ni catalysts have been investigated previously for their high tar cracking activity, e.g., during biomass gasification or bio-oil degradation [9]. They are also commonly used for steam reforming and the partial oxidation of organics, e.g., methanol [10,11], ethanol [5,12] and methane [13]. Ni has been identified as one of the best metals for tar elimination by catalyzing C–C bond breakage; as well as being capable of catalyzing O–H and C–H bond cleavage, and the water–gas shift reaction [7,14–16].

Previous research has shown that the catalyst substrate material and preparation method are critically important. The most common support materials are: γ -Al₂O₃, SiO₂, MgO, ZrO₂ and MgAl₂O₄ [2,9,17–24]. However, the relatively low surface area (mostly less than 200 m²/g) of typical oxide supports can be problematic in terms of achieving an even distribution of catalyst particles on the surface. More recently, mesoporous molecular sieve materials have attracted interest as catalyst supports [5,25,26]. MCM-41 is one of the most promising of these novel support materials, characterized by a highly ordered hexagonal porous structure, a narrow pore size distribution of 2–10 nm, and surface areas of the order of 1000 m²/g – far larger than typical oxide supports. The pore size, which is generally larger than for zeolites, facilitates better mass transfer within the porous structure; and the highly ordered nature of the porous structure promotes a more even distribution of the catalyst particles, which can minimize sintering [27,28].

In this work we investigate the use of Ni catalysts supported on γ -Al₂O₃ and MCM-41 for promoting H₂ selectivity during biomass pyrolysis in dry and wet (where additional water vapour was

* Corresponding author. Tel.: +61 2 9351 2926.

E-mail address: a.harris@usyd.edu.au (A.T. Harris).

introduced) atmosphere. We describe the preparation of the supported catalysts using an incipient wetness impregnation technique, and present experimental results comparing catalyst activity and the influence of catalyst loading on the product gas yield and distribution.

2. Experimental

2.1. Catalyst preparation and characterization

A modified incipient wetness impregnation technique was used to ensure even Ni dispersion on the internal and external surfaces of the support materials. Nickel nitrate ($\text{Ni}(\text{NO}_3)_2 \cdot 6\text{H}_2\text{O}$) was dissolved in twice the usual volume of EtOH needed for incipient wetness, mixed with the support material, and then excess EtOH was evaporated on a mechanical shaker operating at 20 Hz at 25 °C. This mixture was then dried for 4 h under vacuum at 110 °C before it was calcined at 600 °C under N_2 for 4 h. As-synthesized catalysts were reduced under a mixture of 25 vol.% H_2 in N_2 by heating at 10 °C/min to 800 °C and then maintained at 800 °C for 30 min. We then prepared supported catalysts at 5, 10, 15 and 20 wt.% Ni on $\gamma\text{-Al}_2\text{O}_3$ (Sigma–Aldrich, acidic) and MCM-41 (Sigma–Aldrich), respectively. The reduced catalyst and methyl cellulose (Sigma–Aldrich, 99.9%) were combined in a 1:1 mass-ratio in a high-speed vortex mixer and then stored under vacuum prior to reaction.

N_2 adsorption and desorption isotherms (Quantachrome Autosorb-1) were used to determine the surface area and total pore volume according to the BET and BJH models, respectively. The crystalline structure of the supported catalysts was assessed using powder diffraction (SIEMENS D5000 using Cu $\text{K}\alpha$ radiation [$\lambda = 0.1542$ nm] in the 2θ range of 1.0–90° with a scanning step of 0.02°). The average crystal size of the supported Ni particles was estimated using the Scherrer equation [29] and confirmed by transmission electron microscopy (TEM, Philips CM120 BioFilter). Scanning electron microscopy (SEM, XL30) coupled with energy dispersive spectroscopy (EDS) was used to map the particle surface morphology and the distribution of Ni on the supports.

2.2. TG–MS system

The influence of catalyst activity on the pyrolytic decomposition of cellulose was investigated using a modified thermogravimetric analyser (SDT Q600) coupled with a mass spectrometer (ThermoStar GSD301) (TG–MS) described by Florin and Harris [8,30]. The TG–MS measures the sample weight loss during pyrolysis and gasification using a thermobalance sensitive to 0.01 mg. All evolved gases are purged from the reaction zone with Ar (500 ml/min) and a gas sample is delivered via a heated capillary (200 °C) to the MS, which records a mass-spectrum for the evolved species as a function of the decomposition temperature.

Well-mixed cellulose-catalyst samples were loaded into an alumina pan and placed in the TGA furnace. Prior to the commencement of each experiment the furnace was purged with Ar for 1 h to evacuate any air from the reaction zone. Samples were heated at 40 °C/min to 800 °C. A bubbler system was used to inject wet-gas directly into the reaction zone for select experiments; a saturated Ar– H_2O mix was introduced at 50 ml/min with the fraction of H_2O in Ar about 1 vol.%. The consistency of this delivery was monitored by observing the ion current ratio of the major fractions belonging to H_2O ($m/z = 18, 17, 16$) and Ar ($m/z = 40$ and 20).

The m/z numbers recorded for all the ions/ion fragments corresponding to the evolved gas species during the decomposition of cellulose under Ar are given in Table 1. No spectrum was recorded for ions/ion fragments with $m/z > 100$ and we found the background noise level too intense to obtain reliable data for those ion fragments with $m/z > 55$. This suggests that heavier fragments,

Table 1

Key ion fragments and representative gas species.

m/z	Key ion fragments	Representative species
2	H_2^+	Hydrogen
15	CH_3^+	Methane
18	H_2O^+	Water
26,27,41,42,43,55	$\text{C}_2\text{H}_2^+, \text{C}_2\text{H}_3^+, \text{C}_3\text{H}_5^+, \text{C}_3\text{H}_6^+, \text{C}_3\text{H}_7^+, \text{C}_4\text{H}_7^+$	Hydrocarbons
28	CO^+	Carbon monoxide
29	CHO^+	Aldehydes
30	CH_2O^+	Formaldehyde
31,45,46	$\text{CH}_2\text{OH}^+, \text{C}_2\text{H}_5\text{O}^+, \text{C}_2\text{H}_5\text{OH}^+$	Alcohols
44	CO_2^+	Carbon dioxide
2,15,16,18,26,27,28,29, 30, 31,41,42,43,44,45,46,55	–	Total evolved gases

e.g., those derived from tars, were present in very low quantities, or they were not transported via the heated capillary to the MS. Recognizing this limitation of the TG–MS for detecting tars species we estimated the activity of the catalysts for tar decomposition indirectly by determining the changes in the yield and distribution of the permanent gas products.

Reliable TG–MS data was obtained by using small quantities of cellulose (<3 mg) that limited heat and mass transfer effects and minimized the potential for tar blockages in the capillary. The capillary was always positioned 30 mm inside the reaction vessel close to the sample pan such that the temperature at the end of the capillary was heated to the reaction temperature. This also avoided sampling bias. MS detectors were given sufficient time to achieve a steady signal prior to each run and all experiments were conducted on consecutive days to minimize variability in the signal strength associated with normal deterioration of the filament. Despite these measures we observed fluctuations on the MS signals throughout our experimental regime which we attribute to the deterioration of the filament and minor blockages at the end of the capillary due to the presence of condensates. Thus, to eliminate this experimental variability we normalized the raw MS data relative to the stable m/z signals corresponding Ar (i.e., $m/z = 20, 40$) and the weight of cellulose, according to Eq. (1).

Normalized signal for key molecular ions
ion fragments ‘i’

$$= \frac{IC_i}{(IC_{20} + IC_{40}) \times wt(g)} \quad (1)$$

In Eq. (1), ‘ IC_i ’ is the m/z signal for molecular ions/ion fragments i [arbitrary units], ‘ IC_{20} ’ and ‘ IC_{40} ’ are stable m/z signals for Ar, and ‘ wt ’ is the weight of cellulose [g]. The normalized MS ion current signals were expressed as instant volume concentration of the gaseous product in carrier gas (500 ml/min). The generation rate (ml/min/g) was then plotted as a function of reaction temperature (Figs. 6–9) and total gas product (ml/g) was determined by integration of the area under these normalized curves. The integration was performed in the region 200–600 °C, for most of the gaseous yield occurred in this range. This method provides near simultaneous observation of the product gas evolution during cellulose decomposition and a semi-quantitative estimation of the concentration of the product gas species which is comparable across the range of experimental conditions investigated.

The good reproducibility of the thermogravimetric data was concluded by comparing the derivative weight loss profiles for three repeat cellulose pyrolysis experiments. After normalization of the raw ion current signal data, the peaks moved into close alignment demonstrating the effectiveness of the normalization procedure according to Eq. (1) and hence the good reproducibility of the MS data. (This data is given in Supplementary material.)

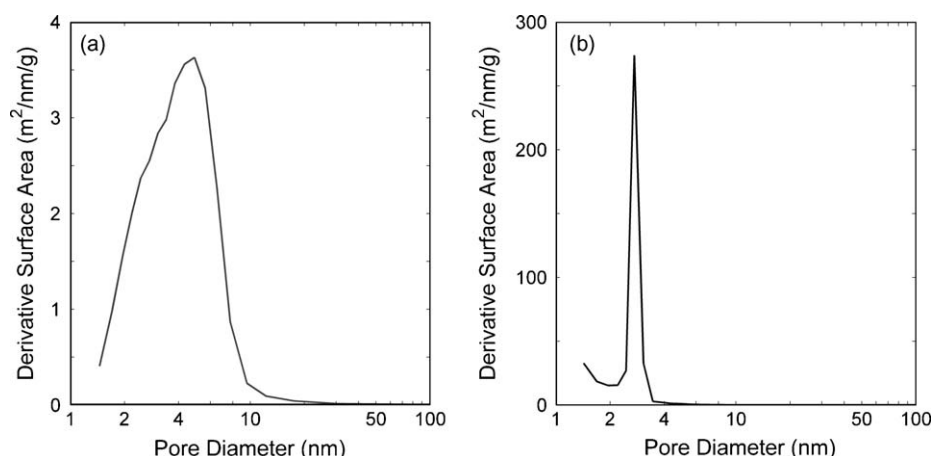


Fig. 1. Pore size distribution for the two support materials measured from N_2 adsorption using the BJH method (log scale for x -axis): (a) γ - Al_2O_3 ; (b) MCM-41.

Table 2

Physical characteristics of supported Ni catalysts.

	Blank support	5%Ni		10%Ni		15%Ni		20%Ni	
		P^a	R^a	P^a	R^a	P^a	R^a	P^a	R^a
γ - Al_2O_3									
S^a	155	122	110	119	113	113	104	109	99
V^a	0.27	0.22	0.20	0.22	0.20	0.20	0.18	0.18	0.16
d^a	8.0	8.4	8.3	8.2	8.5	8.2	8.1	8.1	8.2
MCM-41									
S^a	979	965	914	955	901	942	884	809	789
V^a	0.96	0.95	0.87	0.85	0.79	0.86	0.89	0.72	0.70
d^a	3.9	3.9	3.8	3.6	4.1	3.6	4.0	3.6	3.9

P – precursors of catalysts, R – catalysts reduced under 25% H_2 for 30 min.

^a S – BET surface area (m^2/g), V – pore volume (cm^3/g), d – average pore size (nm).

3. Results and discussion

3.1. Catalyst characterization

γ - Al_2O_3 and MCM-41 are very different in terms of their physical properties (Fig. 1 and Table 2). γ - Al_2O_3 has been widely used as a catalyst support because it is stable, has a large specific surface area and relatively broad pore size distribution. We measured the specific surface area to be $155 m^2/g$, a total pore volume of $0.27 cm^3/g$, and a pore size distribution of 2–8 nm. In comparison, MCM-41 has a significantly greater specific surface area, $979 m^2/g$, a larger pore volume, $0.96 cm^3/g$, and a narrower pore size distribution between 2 and 4 nm.

Changes in the physical properties of the support materials were observed following catalyst impregnation, calcination and reduction (Table 2). The BET surface area and pore volume for both catalysts decreased corresponding to an increase in the metal loading, likely attributable to the filling of some fraction of the pore space with Ni particles. Calcination and reduction caused a 5% decrease in the BET surface areas for both supports, while pore volume and pore size distribution remained constant.

Fig. 2 (right panel) shows wide-angle XRD patterns for 15 wt.% Ni on MCM-41 before (b) and after (a) reduction, and 15 wt.% Ni on γ - Al_2O_3 before (d) and after (c) reduction – allowing a comparison of the nature of the chemical interaction between the Ni catalyst particles and the support materials. Two Ni-phases were identified for the γ - Al_2O_3 supported catalyst, NiO and $NiAl_2O_3$. In the case of the MCM-41, only NiO was identified, suggesting a weaker chemical interaction between Ni and SiO_2 . This is consistent with the lower temperature required to reduce MCM-41 supported

catalysts, about $500^\circ C$ compared to $700^\circ C$ for γ - Al_2O_3 . The weight loss corresponding to the reduction of the supported catalysts measured using the TGA shown in Table 3, supports the quantitative estimates of the NiO-phase based on XRD.

Fig. 2 (left panel) shows small-angle XRD patterns for MCM-41 for 0, 5, 10, and 15% Ni loadings (a–d, respectively). The impregnation of Ni in the MCM-41 pore structure resulted in some deterioration of the ordered hexagonal pore structure, evidenced by the broadening of the diffraction peak (1 0 0) and a decrease in the intensity of peaks (1 1 0 and 2 0 0) [33]—this trend was exaggerated corresponding to an increase in the Ni content.

Fig. 3 shows SEM images for 5 wt.% Ni on γ - Al_2O_3 (a) and MCM-41 (c), respectively. These two images were also used for the area EDS scanning with spectrum displayed in (b) and (d) and multi-spot EDS scanning carried out in the four labeled locations with the corresponding Ni wt.% distributions together with the average

Table 3

Reducibility of catalysts precursors.

	5%Ni	10%Ni	15%Ni	20%Ni
Stoichiometric weight loss	1.34%	2.64%	3.91%	5.14%
γ - Al_2O_3				
Weight loss in TG	2.07%	2.93%	4.27%	5.04%
Peak temp ($^\circ C$)	700	710	680	658
MCM-41				
Weight loss in TG	1.45%	3.05%	4.12%	4.85%
Peak temp ($^\circ C$)	495	500	495	510

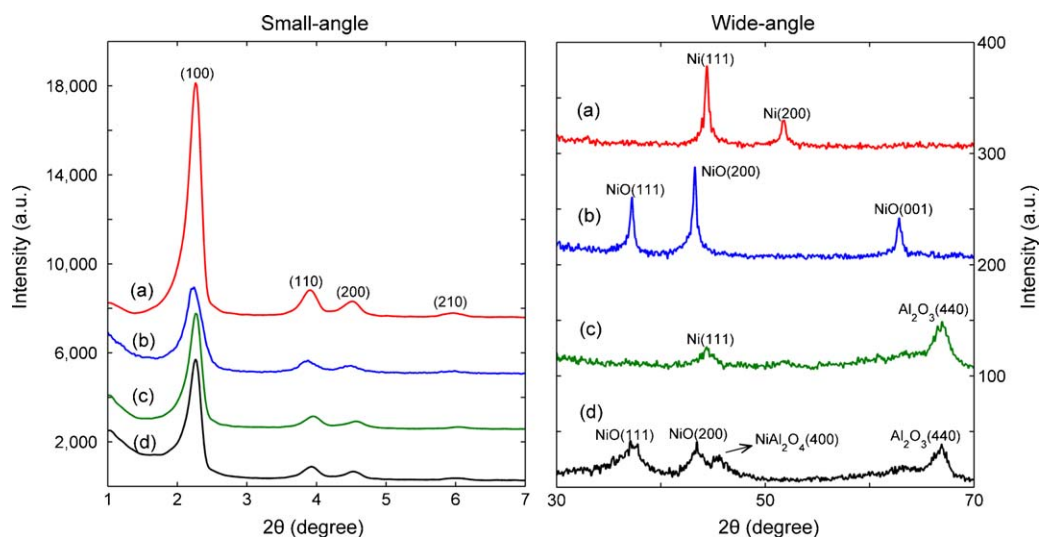


Fig. 2. Small-angle XRD patterns (left panel) for MCM-41 supported Ni catalysts (all reduced under H_2 for 30 min): (a) blank MCM-41; (b) 5 wt.% Ni on MCM-41; (c) 10 wt.% Ni on MCM-41; (d) 15 wt.% Ni on MCM-41; wide-angle XRD patterns (right panel): 15 wt.% Ni on MCM-41 after reduction (a) and before reduction (b); 15 wt.% Ni on γ - Al_2O_3 after reduction (c) and before reduction (d).

percentage of the area presented in the accompanying table in (b) and (d) by the quantitative function of EDS.

We chose to use different magnification levels for the above analysis because the porous structure of γ - Al_2O_3 occurs at a markedly different scale to that of MCM-41. Fig. 3-a (at a magnification of 5000 \times) is appropriate to show the disordered

surface morphology of 5 wt.% Ni supported on γ - Al_2O_3 , indicating that the metal sites are concentrated around the gaps between the γ - Al_2O_3 particles; the great magnification used to study the porous structure of the MCM-41 supported catalysts (50,000 \times) cannot reflect the full view of the wall-gap structure in this instance. The disorder is confirmed by the Ni wt.% determined by EDS whereby

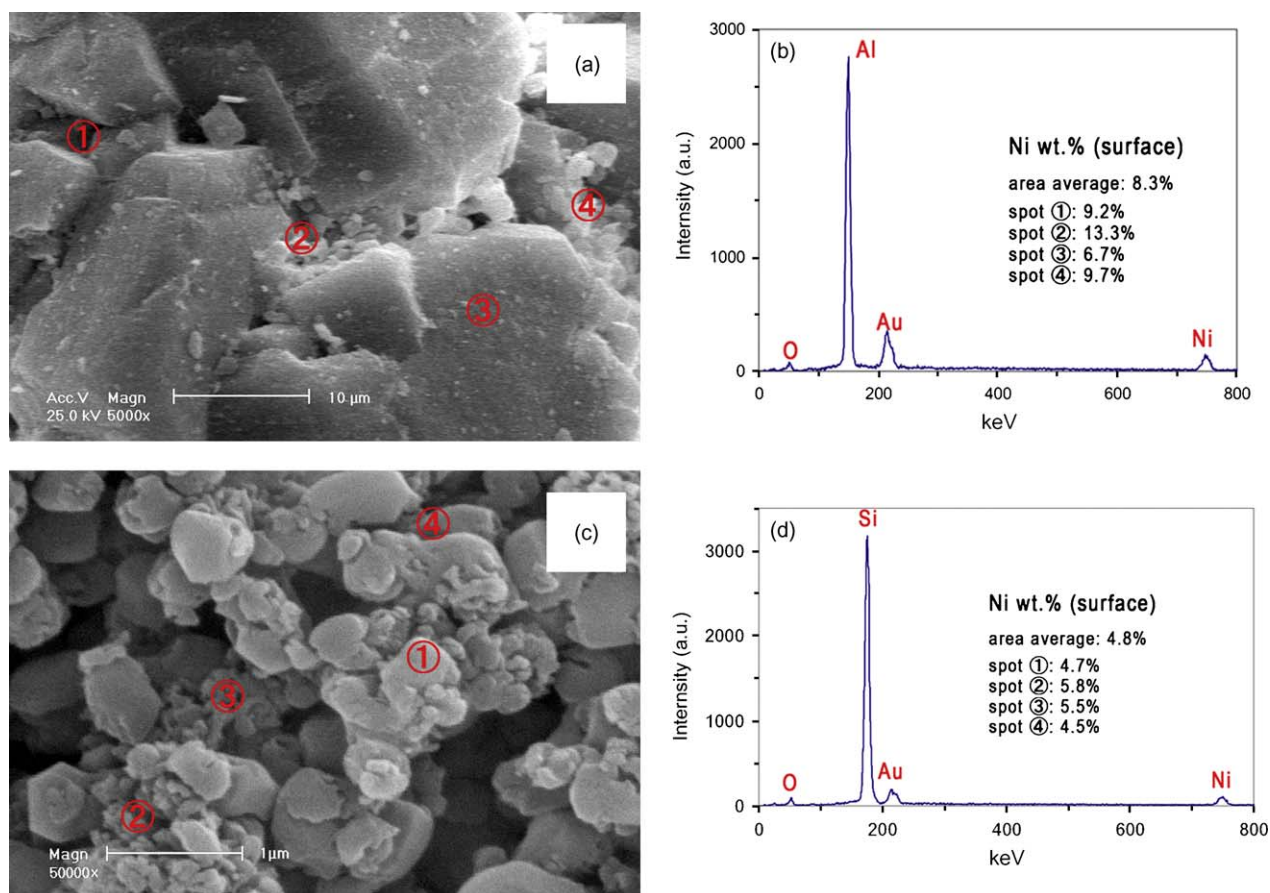


Fig. 3. Scanning electron micrographs for (a) blank γ - Al_2O_3 and (c) 5 wt.% Ni on γ - Al_2O_3 , and corresponding energy dispersive X-ray spectroscopy (b) and (d) with quantitative analysis of area and spot EDS given in accompanying tables.

only 6.7 wt.% was measured at location 3 on the surface of a γ - Al_2O_3 particle, compared to 13.3 wt.% at location 2 shown in the gap between support particles. Contrastively, Fig. 3-c at a magnification of 50,000 \times shows the ordered porous structure characteristic of 5 wt.% Ni supported on MCM-41. No significant deterioration was observed as a result of catalyst impregnation compared to the morphology of blank support material. It is apparent that the highly ordered structure facilitates the even distribution of the Ni catalyst particles; this is confirmed by EDS showing consistent quantities of Ni in the 4 locations. Furthermore, location 3, which is positioned within a large open cavity, suggests that the distribution of Ni is not limited to the outer surface of the support material. Consistent results were achieved during numerous repeat experiments using this methodology for the MCM-41 catalyst at a magnification of 50,000 \times .

Further information regarding the porous structure of Ni catalyst supported on MCM-41 was obtained using TEM. Fig. 4a–d shows TEM images for the MCM-41 support without impregnated Ni, and with 5, 10 and 15 wt.% Ni loadings. Fig. 4-a shows the highly ordered mesoporous structure, which appears in a regular hexagonal arrangement with a pore size of about 3–4 nm, consistent with the pore size analysis based on N_2 adsorption (Table 2). Upon catalyst particle impregnation, the Ni particles appear as small nano-sized dark spots, which grow in size corresponding with an increase in the Ni loading from 5 to 15 wt.% (Fig. 4b–d). With a 5 wt.% Ni loading the Ni particles appear to be regular in shape, well distributed and about the same size as the pores in the MCM-41. However, at the higher loadings some of the Ni particles appear to merge resulting in an uneven distribution of particles and a broad range of particle sizes. These results may indicate that there is an optimal catalyst loading to promote an even distribution of uniformly sized catalyst particles.

3.2. Catalyst tests using TGA–MS

3.2.1. Hydrogen and total gas production

Cellulose is a glucose polymer, consisting of linear chains of (1,4)-D-glucopyranose units, in which the units are linked 1–4 in the β -configuration, with an average molecular weight of around 100,000 [4]. When heated this chain structure decomposes and evolved species react further as shown in Table 4, which lists the main gas-phase reactions [8,23,31,32]. Ni catalysts are expected to influence product gas quantity and composition in three main ways: (i) improving tar cracking reactions by catalyzing C–C bond cleavage; (ii) enhancing the reforming of light gas molecules, e.g., breaking C–H bonds; and (iii) enhancing the water–gas shift reaction towards maximizing the consumption of CO.

Fig. 5 compares the influence of eight supported Ni catalysts on the accumulative H_2 yields measured during pyrolytic decomposition from 200 to 600 °C in pure and wet Ar (1 vol.% of steam), respectively. More data on total gas yield and distribution is given in Tables 5 and 6, which also includes the quantity of residue char (wt.%) at 600 °C. As stated in Section 2.2, gas yields were calculated by integration of normalized signal that was further converted to generation rates between 200 and 600 °C and expressed with the unit of ml/g cellulose that is far larger than the volume at normal conditions (room temperature). Thus this data cannot be regarded as real production but comparable between the different experiment conditions.

In the absence of catalyst, the total gas yield for cellulose pyrolysis was about 700 ml/g consisting of 1.2 vol.% H_2 , presumably derived solely from direct thermal decomposition of the cellulose. The presence of Ni supported on γ - Al_2O_3 resulted in an average increase in the average value of total gas production by about 25 vol.%. A significantly greater increase in the total gas

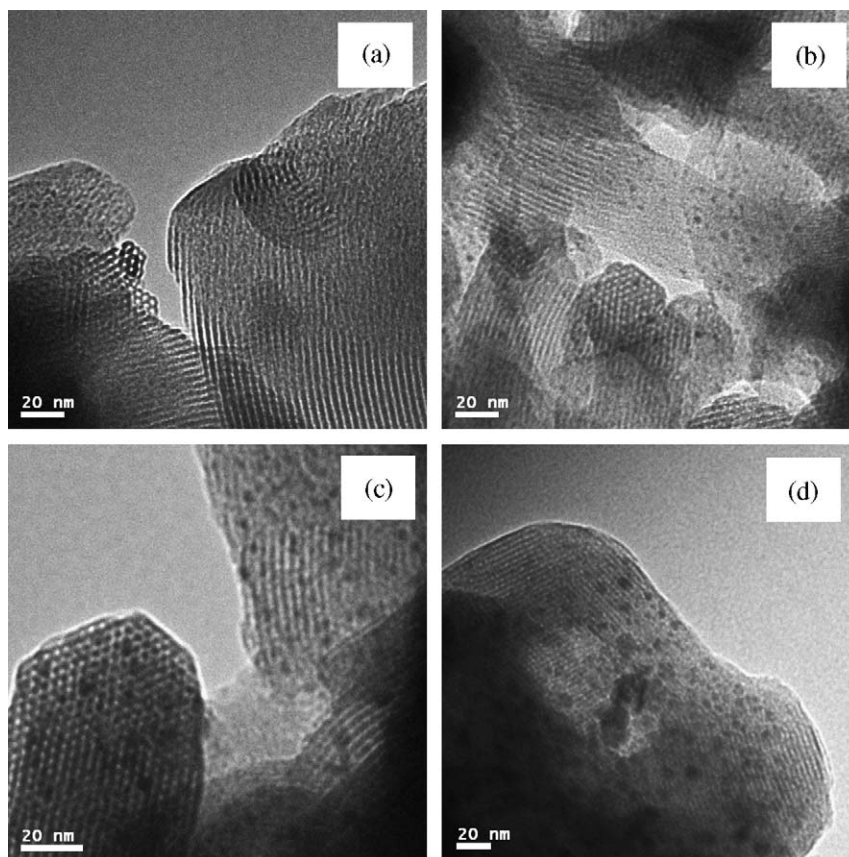
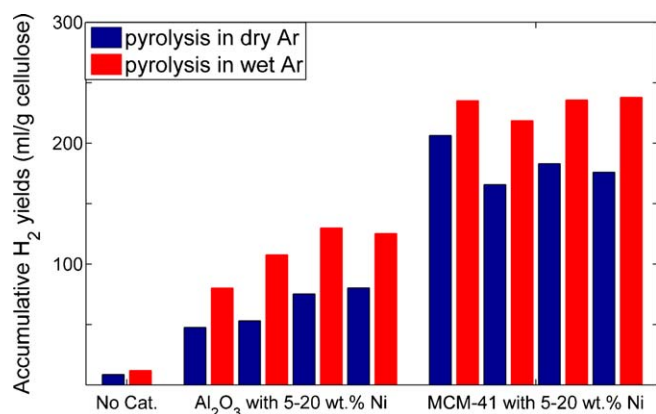


Fig. 4. Transmission electron images of (a) blank MCM-41, (b) 5 wt.% Ni on MCM-41, (c) 10 wt.% Ni on MCM-41, and (d) 15 wt.% Ni on MCM-41.

Table 4

Main gas-phase reactions of catalytic biomass (cellulose) pyrolysis/gasification.

Reaction	Equation	$\Delta H_{298.15}^\circ$ (kJ/mol)
Thermal decomposition	$\text{Biomass} \rightarrow \text{H}_2\text{O} + \text{H}_2 + \text{CO} + \text{CO}_2 + \text{organic volatiles} + \text{volatile tars} + \text{char}$ (2)	–
Tars cracking (catalytic)	$\text{Tars} \rightarrow \text{H}_2\text{O} + \text{H}_2 + \text{CO} + \text{CO}_2 + \text{CH}_4 + \text{C}_x\text{H}_y + \text{C}_2\text{H}_5\text{OH} + \text{CH}_3\text{OH} + \text{CH}_2\text{O} + \text{CH}_3\text{CHO}$ (3)	–
Catalytic cracking	$\text{C}_2\text{H}_5\text{OH} \rightarrow \text{CH}_3\text{CHO} + \text{H}_2$ (4)	+225.0, Endothermic
Catalytic cracking	$\text{CH}_3\text{CHO} \rightarrow \text{CH}_4 + \text{CO}$ (5)	–132.8, Exothermic
Catalytic cracking	$\text{CH}_2\text{O} \rightarrow \text{CO} + \text{H}_2$ (6)	+5.4, Endothermic
Water-gas shift	$\text{CO} + \text{H}_2\text{O} \rightarrow \text{CO}_2 + \text{H}_2$ (7)	–41.1, Exothermic
Steam reforming	$\text{CH}_4 + \text{H}_2\text{O} \rightarrow \text{CO} + 3\text{H}_2$ (8)	+206.2, Endothermic
Steam reforming	$\text{C}_x\text{H}_y + x\text{H}_2\text{O} \rightarrow x\text{CO} + (n + 0.5m)\text{H}_2$ (9)	Endothermic

**Fig. 5.** Accumulative H₂ yields for pyrolysis in dry and wet Ar with different catalysts (200–600 °C).

production up to about 70 vol.% was observed using Ni supported on MCM-41. The dramatic increase in the total gas yield demonstrates the activity of the Ni catalysts for the decomposition of tar, in accordance with the reactions presented in Table 4. A substantial increase in the hydrogen output (Fig. 5) and the total gas yield (Table 5) were also observed to accompany the

introduction of additional water vapour. The influence of additional water vapour is discussed in Section 3.2.3.

During pyrolysis, without additional water vapour, we observed an increasing trend in the H₂ output corresponding with an increase in the Ni loading when supported by γ -Al₂O₃. When additional water vapour was introduced, we identified a maximum H₂ output with 15 wt.% Ni on γ -Al₂O₃. Under these experimental conditions, we recorded the highest CO and lowest CO₂ outputs. No clear trend was observed regarding the H₂ output with increasing Ni catalyst loading on MCM-41—either in the presence or absence of additional water vapour. However, we did observe an increase in the H₂ output when additional water vapour was introduced at all loadings; and the H₂ output was consistently greater for Ni catalysts on MCM-41, compared with γ -Al₂O₃. On the basis of the fact that we observed the highest H₂ outputs with 15 wt.% Ni on γ -Al₂O₃ (80.2 ml/g-cellulose), and with 5 wt.% Ni on MCM-41 (235.7 ml/g-cellulose), these catalysts were selected for all subsequent investigation.

3.2.2. Influence of substrate material on evolved species

Figs. 6 and 7 display how the two selected Ni catalysts influence the kinetics of cellulose pyrolysis in terms of the rate of generation of H₂, CO₂, CO, CH₄ and C_xH_y, respectively. Fig. 6-b is included to show the derivative weight loss curve for cellulose mixed with 15 wt.% Ni on γ -Al₂O₃, and 5 wt.% Ni on MCM-41, respectively.

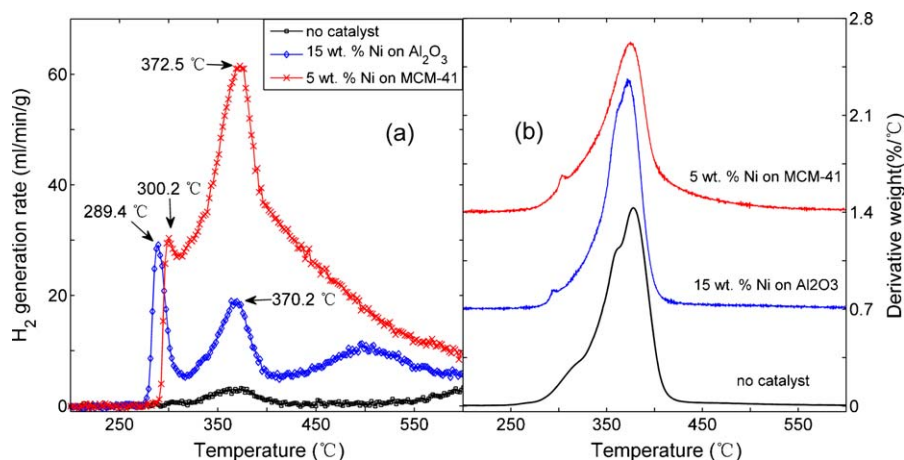
Table 5Total gas^a and char yields and product gas distribution during pyrolysis in pure Ar.

	Product gas distribution (vol.%)								Total gas yield (ml/g cellulose)	Char yield (wt.%)
	H ₂	CO ₂	CO	CH ₄	C _x H _y	CH ₃ CHO	CH ₂ O	CH ₃ OH, C ₂ H ₅ OH		
Pure cellulose	1.2	23.8	32.9	6.6	3.1	17.4	9.4	5.6	722.5	14.6
Al ₂ O ₃	1.5	25.9	31.3	5.8	3.0	17.4	10.5	4.6	850.3	14.4
5%Ni/Al ₂ O ₃	5.2	24.0	32.6	4.5	3.3	16.2	9.2	5.0	918.6	12.4
10%Ni/Al ₂ O ₃	5.8	25.1	33.0	4.3	3.0	15.5	8.7	4.6	913.0	11.9
15%Ni/Al ₂ O ₃	8.6	21.4	35.6	4.4	3.2	14.5	8.3	4.0	873.0	11.6
20%Ni/Al ₂ O ₃	9.0	22.7	33.4	4.8	3.2	14.4	8.4	4.1	895.8	13.5
MCM-41	1.8	21.0	33.0	7.0	4.6	17.6	9.0	6.0	965.9	14.5
5%Ni/MCM-41	16.5	18.1	42.4	3.4	2.8	9.0	5.2	2.5	1249.1	13.4
10%Ni/MCM-41	13.4	19.5	40.1	3.8	3.1	10.4	6.3	3.4	1240.6	14.4
15%Ni/MCM-41	15.4	17.7	41.0	3.6	2.9	10.2	6.1	3.0	1186.6	14.4
20%Ni/MCM-41	14.4	18.1	40.2	3.8	2.8	11.2	6.2	3.3	1224.6	14.1

^aEvolved H₂O was excluded in total gas.

Table 6Total gas^a and char yields and product gas distribution during pyrolysis in wet Ar.

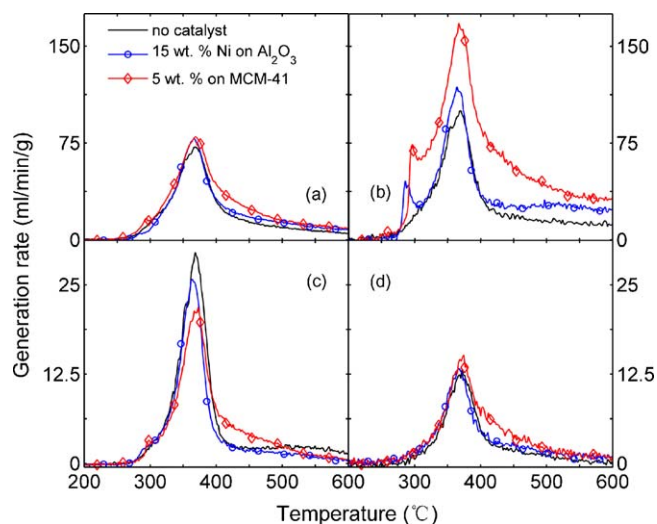
	Product gas distribution (vol.%)								Total gas yield (ml/g cellulose)	Char yield (wt.%)
	H ₂	CO ₂	CO	CH ₄	C _x H _y	CH ₃ CHO	CH ₂ O	CH ₃ OH, C ₂ H ₅ OH		
Pure cellulose	1.2	25.2	31.6	6.0	2.7	17.7	9.2	6.4	1032.8	13.88
5%Ni/Al ₂ O ₃	7.4	23.9	25.5	4.9	2.5	18.9	10.8	6.0	1105.3	12.97
10%Ni/Al ₂ O ₃	9.7	23.6	32.2	4.1	2.1	15.5	7.6	5.1	1120.0	12.56
15%Ni/Al ₂ O ₃	11.6	20.1	34.7	4.4	2.8	14.5	7.7	4.2	1122.6	11.98
20%Ni/Al ₂ O ₃	10.1	26.2	28.1	4.8	2.6	15.0	8.4	4.8	1241.4	12.28
5%Ni/MCM-41	18.8	23.1	34.2	3.4	2.0	9.6	5.6	3.3	1250.6	10.72
10%Ni/MCM-41	16.7	20.3	36.2	3.8	2.2	10.8	6.4	3.6	1308.1	12.52
15%Ni/MCM-41	17.1	19.2	38.0	3.5	2.2	10.4	5.9	3.6	1378.3	11.32
20%Ni/MCM-41	17.0	18.4	39.6	3.3	2.0	10.3	5.8	3.4	1398.0	11.55

^a Evolved H₂O was excluded in total gas.**Fig. 6.** Influence of catalyst substrate material on (a) H₂ generation rate and (b) decomposition weight loss profile during pyrolysis in dry Ar.

The derivative weight loss peaks, e.g., Fig. 6-b, indicated that nearly all product gas species were evolved during heating from 200 to 600 °C. At 600 °C the final char residue was observed to show a similar trend with total gas yield between different conditions (Tables 5 and 6) indicating that the catalysts ordinarily affect the char gasification reactions. In addition, extra steam did help to reduce the residue char, and in 1 vol.% wet Ar, 15 wt.% Ni on γ -Al₂O₃ and 5 wt.% Ni on MCM-41 presented the lowest residue ratio to 12.0 wt.% and 10.7 wt.%, respectively, which was decreased compared with no catalyst in dry Ar (14.6 wt.%). A significant

decrease in the temperature corresponding to the main derivative weight loss peak, and the emergence of a new minor peak at low temperatures – observable in all experiments when catalysts were present – demonstrate the activity of Ni catalysts for promoting the pyrolytic decomposition of cellulose. Specifically, the derivative weight loss curve for pure cellulose was characterized by a single distinct peak with the maximum rate of weight loss at 378 °C, which is consistent with previous studies [8]. This decomposition may be explained according to Eq. (2) (Table 4). A decrease in the temperature corresponding to the maximum rate of weight loss was observed to 370 °C and 373 °C with 15 wt.% Ni on γ -Al₂O₃ and 5 wt.% Ni on MCM-41, respectively. In addition, we observed a secondary peak at 289 °C and 300 °C for the γ -Al₂O₃ and MCM-41 supported catalysts, in turn. The low temperature secondary peaks corresponded exclusively with the evolution of H₂ and CO. Thus, according to the reactions presented in Table 4, it is likely that the shift in the primary peak is attributable to catalytically enhanced cracking reactions given by Eqs. (3)–(6), with very large equilibrium constants around 300 °C [5]. The emergence of the secondary peak may be attributed to the promotion of reactions given by Eqs. (5) and (6).

The temperature corresponding to the maximum rate of H₂ evolution (including both primary and secondary peaks) for 15 wt.% Ni on γ -Al₂O₃ was marginally lower compared with 5 wt.% Ni on MCM-41. However, the temperature corresponding to the commencement of the smaller, low temperature peak, i.e., for Ni supported on γ -Al₂O₃, the H₂-evolution peak starts at about 25 °C lower compared with Ni on MCM-41. This is due to surface acidity of γ -Al₂O₃ which promoted the tars cracking reactions [23]. The greater capacity of the Ni catalyst on MCM-41 for elevating the output of H₂ may be attributed to the highly ordered mesoporous structure, which promotes Ni dispersion; and thus, increases the

**Fig. 7.** Influence of catalyst substrate material on generation rates of (a) CO₂, (b) CO, (c) CH₄, and (d) C_xH_y during pyrolysis in dry Ar.

interaction between active Ni sites and the gas molecules. This enhanced interaction maximizes secondary decomposition reactions leading to higher H_2 yield.

We observed a third peak corresponding to the evolution of H_2 for 15 wt.% Ni on $\gamma\text{-Al}_2\text{O}_3$ with the maximum rate of evolution at 502.1 °C. We were unable to determine whether this unique H_2 -evolution event occurred with 5 wt.% Ni on MCM-41 because of the lagging decline in the tail of the primary peak. However, it is likely that the lagging decline in the tail corresponds with a H_2 production mechanism which is important across a broad temperature range from 400 to 500 °C. Gas evolution profiles, similar to those shown for H_2 , were observed with both catalysts corresponding to the evolution of CO and CH_4 , shown in Fig. 7-b and -c, respectively. These results are consistent with the reaction mechanism according to Eqs. (3)–(6). The CO output was significantly increased by the presence of Ni on MCM-41 and a corresponding decrease in the yields of CH_4 , aldehydes and alcohols were observed (Tables 5 and 6). These findings may be explained in terms of a high activity of Ni catalysts for promoting the cracking and reforming reactions given by Eqs. (4)–(6) and (8) (Table 4). By contrast, the influence of the supported Ni catalysts on the decomposition of higher hydrocarbons, i.e., C_xH_y , was less pronounced.

3.2.3. Influence of additional water vapour

The presence of additional water vapour, during pyrolysis with 15 wt.% Ni on $\gamma\text{-Al}_2\text{O}_3$, affected the output of H_2 in three main ways (Fig. 8-a): Firstly, there was a delay in the initial evolution of H_2 by about 25 °C. Secondly, the delay in the low temperature peak caused it to merge with the peak observed around 350–400 °C resulting in one broad peak spanning the temperature range from 300 to 400 °C. Finally – and most significantly – the H_2 evolution at about 500 °C was significantly promoted by the presence of additional water vapour, which is likely attributable to the promotion of the endothermic reforming reactions, according to Eqs. (8) and (9). In Fig. 8-b, with 5 wt.% Ni on MCM-41, we observed a similar delay in the initial evolution of H_2 , however the primary peaks corresponding the maximum rate of H_2 evolution were closely aligned both with and without additional water vapour. The lagging decline in the tail of the primary peak was even more pronounced, again consistent with the promotion of the endothermic reforming reactions, according to Eqs. (8) and (9). The different H_2 -evolution profiles shown in Fig. 8a and b for the two selected

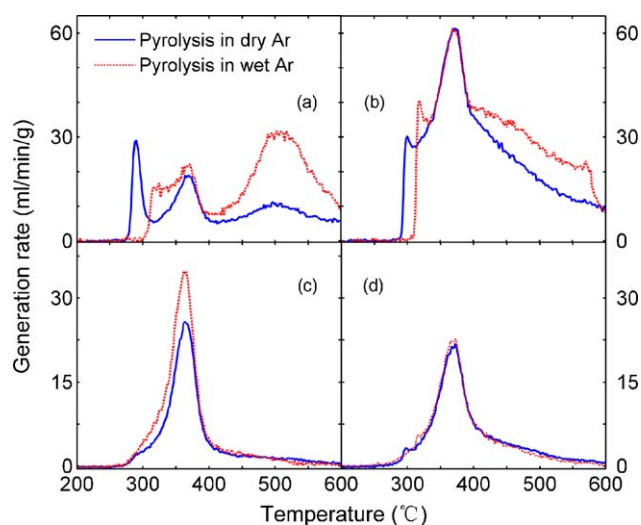


Fig. 8. Influence of additional water vapour on H_2 generation rate with (a) 15 wt.% Ni on $\gamma\text{-Al}_2\text{O}_3$ and (b) 5 wt.% Ni on MCM-41, and on CH_4 generation rate with (c) 15 wt.% Ni on $\gamma\text{-Al}_2\text{O}_3$ and (d) 5 wt.% Ni on MCM-41.

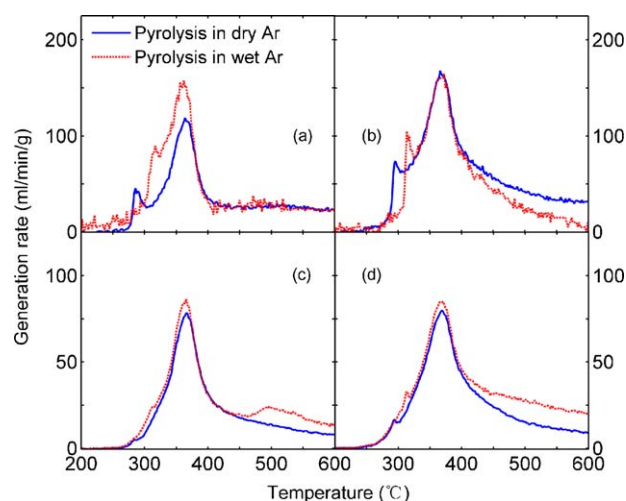


Fig. 9. Influence of additional water vapour on CO generation rate with (a) 15 wt.% Ni on $\gamma\text{-Al}_2\text{O}_3$ and (b) 5 wt.% Ni on MCM-41, and on CO_2 generation rate with (c) 15 wt.% Ni on $\gamma\text{-Al}_2\text{O}_3$ and (d) 5 wt.% Ni on MCM-41.

catalysts suggest that different H_2 production mechanisms are dominant during the pyrolytic decomposition of cellulose. Cellulose pyrolysis with 15 wt.% Ni on $\gamma\text{-Al}_2\text{O}_3$ appears to be most sensitive to the introduction of additional water vapour.

Fig. 9 shows the rate of evolution of CO and CO_2 , with and without additional water vapour, respectively. We observed a small increase in the output of CO with 15 wt.% Ni on $\gamma\text{-Al}_2\text{O}_3$ in the presence of additional water vapour during decomposition from 300 to 400 °C (Fig. 9-a). In contrast, the amount of CO evolved with 5 wt.% Ni on MCM-41 was lower in the high-temperature range, i.e., >400 °C, when additional water vapour was introduced (Fig. 9-b). Both catalysts promoted an increase in the output of CO_2 reflected by the small increase in the primary peak and a slower decline in the peak tail when additional water vapour was present. A parallel decrease in CO and an increase in H_2 and CO_2 with 5 wt.% Ni on MCM-41 was observed at temperatures >400 °C, which is consistent with the promotion of the water–gas shift reaction. Higher content of CH_4 with 15 wt.% Ni on $\gamma\text{-Al}_2\text{O}_3$ also contributed to the increase of CO according to Fig. 8-c. On the other hand, a low CH_4 concentration suggested better catalyzing activity of 5 wt.% Ni on MCM-41 on steam reforming reactions.

4. Conclusions

An incipient wetness impregnation technique was developed to load Ni catalyst onto $\gamma\text{-Al}_2\text{O}_3$ and MCM-41 supports. The highly ordered mesoporous structure of the MCM-41 was superior in terms of obtaining an even distribution of catalyst particles throughout the support material. In the case of MCM-41, a 5 wt.% Ni loading resulted in an even distribution of Ni particles that were regular in shape and about the same size as the pores in the support; however, at the higher loadings the Ni particles coalesced resulting in an uneven distribution of particles and a broad range of active catalyst particle sizes. The distribution of catalyst particles on the support was closely reflected in the observed activity of the catalysts for maximizing gas yields, presumably due to enhanced contact between Ni sites and the evolved species resulting in advanced secondary decomposition. Correspondingly, the MCM-41 supported catalysts displayed a much higher activity for tar and light organic cracking and reforming compared with $\gamma\text{-Al}_2\text{O}_3$ supported catalysts. Conversely, the acidity of $\gamma\text{-Al}_2\text{O}_3$ support and the interaction between Ni and Al_2O_3 may be advantageous for promoting endothermic reforming reactions. We achieved the

highest H₂ yield, H₂ selectivity and total gas yield with 5 wt.% Ni on MCM-41. An increase in CO in parallel with the enhanced H₂ output, up to about 35 vol.% (dry), was observed with all catalysts. On one hand, this was resulting from the case that there is insufficient residence time to achieve thermodynamic equilibrium due to the rapid purging of the TGA furnace with Ar; on the other hand, it also highlighted the scope for further modification of catalysts to promote the water–gas shift reaction.

Acknowledgements

MZ is grateful to the Chinese Scholarship Council and the University of Sydney for a postgraduate scholarship. The authors are grateful for the assistance Dr. J. Shi and S. Bulcock for assistance with operation of the XRD and the acquisition of SEM and TEM images, respectively. This work was funded, in part, by the Australian Research Council under DP0666488.

Appendix A. Supplementary data

Supplementary data associated with this article can be found, in the online version, at [doi:10.1016/j.apcatb.2009.07.011](https://doi.org/10.1016/j.apcatb.2009.07.011).

References

- [1] P. McKendry, *Bioresour. Technol.* 83 (2002) 47–54.
- [2] M. Asadullah, T. Miyazawa, S.-i. Ito, K. Kunimori, M. Yamada, K. Tomishige, *Appl. Catal. A-Gen.* 255 (2003) 169–180.
- [3] N.H. Florin, A.T. Harris, *Chem. Eng. Sci.* 63 (2008) 287–316.
- [4] P. McKendry, *Bioresour. Technol.* 83 (2002) 37–46.
- [5] E. Ozdogan, *Int. J. Chem. React. Eng.* 5 (2007).
- [6] T. Hanaoka, T. Yoshida, S. Fujimoto, K. Kamei, M. Harada, Y. Suzuki, H. Hatano, S.-y. Yokoyama, T. Minowa, *Biomass Bioenergy* 28 (2005) 63–68.
- [7] D. Sutton, B. Kelleher, J.R.H. Ross, *Fuel Process. Technol.* 73 (2001) 155–173.
- [8] N.H. Florin, A.T. Harris, *AIChE J.* 54 (2008) 1096–1109.
- [9] T. Kimura, T. Miyazawa, J. Nishikawa, S. Kado, K. Okumura, T. Miyao, S. Naito, K. Kunimori, K. Tomishige, *Appl. Catal. B-Environ.* 68 (2006) 160–170.
- [10] Y. Matsumura, H. Ishibe, *Appl. Catal. B-Environ.* 91 (2009) 524–532.
- [11] S.D. Jones, L.M. Neal, H.E. Hagelin-Weaver, *Appl. Catal. B-Environ.* 84 (2008) 631–642.
- [12] M.A. Goula, S.K. Kontou, P.E. Tsiakaras, *Appl. Catal. B-Environ.* 49 (2004) 135–144.
- [13] F. Pompeo, N.N. Nichio, M.M.V.M. Souza, D.V. Cesar, O.A. Ferretti, M. Schmal, *Appl. Catal. A-Gen.* 316 (2007) 175–183.
- [14] J. Han, H. Kim, *Renew. Sust. Energy Rev.* 12 (2008) 397–416.
- [15] D.C. Grenoble, M.M. Estadt, D.F. Ollis, *J. Catal.* 67 (1981) 90–102.
- [16] R.R. Davda, J.W. Shabaker, G.W. Huber, R.D. Cortright, J.A. Dumesic, *Appl. Catal. B-Environ.* 56 (2005) 171–186.
- [17] R. Zhang, Y. Wang, R.C. Brown, *Energy Convers. Manage.* 48 (2007) 68–77.
- [18] C. Wu, P.T. Williams, *Appl. Catal. B-Environ.* 87 (2009) 152–161.
- [19] T. Wang, J. Chang, P. Lv, J. Zhu, *Energy Fuels* 19 (2005) 22–27.
- [20] D. Swierczynski, C. Courson, L. Bedel, A. Kiennemann, J. Guille, *Chem. Mater.* 18 (2006) 4025–4032.
- [21] J.G. Seo, M.H. Youn, I.K. Song, *J. Power Sources* 168 (2007) 251–257.
- [22] F. Pompeo, N.N. Nichio, O.A. Ferretti, D. Resasco, *Int. J. Hydrog. Energy* 30 (2005) 1399–1405.
- [23] J. Li, R. Yan, B. Xiao, D.T. Liang, L. Du, *Environ. Sci. Technol.* 42 (2008) 6224–6229.
- [24] L. Garcia, R. French, S. Czernik, E. Chornet, *Appl. Catal. A-Gen.* 201 (2000) 225–239.
- [25] Z. Mu, J.J. Li, H. Tian, Z.P. Hao, S.Z. Qiao, *Mater. Res. Bull.* 43 (2008) 2599–2606.
- [26] J. Adam, M. BlazsÜ, E. Mész-ros, M. Stocker, M.H. Nilsen, A. Bouzga, J.E. Hustad, M. Gronli, G. Oye, *Fuel* 84 (2005) 1494–1502.
- [27] S. Todorova, V. Pârvulescu, G. Kadinov, K. Tenchev, S. Somacescu, B.L. Su, *Micropor. Mesopor. Mater.* 113 (2008) 22–30.
- [28] Á. Szegedi, M. Popova, V. Mavrodinova, C. Minchev, *Appl. Catal. A-Gen.* 338 (2008) 44–51.
- [29] A.L. Patterson, *Phys. Rev.* 56 (1939) 978–982.
- [30] N.H. Florin, A.T. Harris, *Energy Fuels* 22 (2008) 2734–2742.
- [31] H. Yang, R. Yan, H. Chen, D.H. Lee, C. Zheng, *Fuel* 86 (2007) 1781–1788.
- [32] M.J. Antal Jr., G. Varhegyi, *Ind. Eng. Chem. Res.* 34 (1995) 703–717.
- [33] E.F. Iliopoulou, E.V. Antonakou, S.A. Karakoulia, I.A. Vasalos, A.A. Lappas, K.S. Triantafyllidis, *Chem. Eng. J.* 134 (2007) 51–57.